nature energy

Article

https://doi.org/10.1038/s41560-026-01974-2

Durable alloy anode for Na-ion batteries with high volumetric energy density

Received: 3 April 2025

Accepted: 6 January 2026

Published online: 16 February 2026

Check for updates

Zhao Chen[1,2,6], Yuqi Li[1,2,5,6], Liqi Wang[1,2], Jiao Zhang[1,3], Rongbin Dang[1,3], Hailong Yu[1,3], Bowen Wang[1], Chunliu Xu[1], Huajun Li[1,2,3], Yuting Li[1], Yu Li[1,2,3], Lin Zhou[1], Fei Xie[1] ✉, Ruijuan Xiao[1,2], Yaxiang Lu[1,3], Hong Li[1,2], Xuejie Huang[1,2], Liquan Chen[1,2] & Yong-Sheng Hu[1,2,3,4] ✉

Alloy anodes can offer high energy densities of Na-ion batteries (NIBs) but suffer from poor cycling performance. Conventional strategies to mitigate the volume expansion often sacrifice the capacity delivery and material scalability, while the underlying mechanisms governing the cycling stability and practical applicability remain unrevealed. Here we design a scalable micrometre-scale Sn anode for ampere-hour-level NIBs, which delivers a high volumetric energy density of 453 Wh l^{-1} and realizes fast charging (~15 min) over 600 cycles. Notably, the Sn-based cell exhibits superior low-temperature performance compared with the $LiFePO_4$/graphite cell. Multiscale characterizations combined with machine learning-assisted quantitative analyses reveal that the adequate and continuous topological morphological evolution of the Sn particles, synergistically reinforced by the cross-linked networks of single-walled carbon nanotubes, ensures stable electrical connection and high active material utilization throughout the cycle life. This work clarifies the structure–stability–performance correlation of alloy-based anodes and highlights their great potential for next-generation high-energy NIBs.

Na-ion batteries (NIBs) have entered a critical stage of commercial development based on their great potential in large-scale energy storage and electrical heavy trucks. However, the space and volume requirements of these application scenarios put forward higher demand on not only the mass energy density but also more on volumetric energy density. To achieve this goal, alloy-based anodes such as Sn present as a promising candidate. In addition to having high theoretical capacity and compacted density, they are safer and easier to handle than the metallic Na anodes, and can be prepared under air, which are compatible with existing production lines, thus showing better practical prospects[1,2]. However, the Sn anodes are suffering from poor cycling stability. The substantial volume change during cycling leads to gradual particle pulverization[3], resulting in the sluggish dynamics and severe capacity fading[1,4–6,2]. Moreover, the insufficient Mohs hardness of Sn can cause spontaneous agglomeration during slurry preparation, hindering the potential of practical cell fabrication.

In reality, the core of the serious capacity fading of alloy-based anodes is not the volume expansion itself, but the derivative formation of electrical isolated 'dead' particles upon the volume expansion, leading to the electrical connection loss among the active particles and the pulverization of the electrodes. Numerous studies have explored various modification strategies, such as nano-sizing particles[7,8], designing special morphologies[9–11], compositing with carbonaceous matrix[12–18], optimizing electrolytes[19–24] and incorporating new binders[25,26], which

[1]Key Laboratory for Renewable Energy, Beijing Key Laboratory for New Energy Materials and Devices, Beijing National Laboratory for Condensed Matter Physics, Institute of Physics, Chinese Academy of Sciences, Beijing, China. [2]College of Materials Science and Optoelectronic Technology, University of Chinese Academy of Sciences, Beijing, China. [3]Huairou Division, Institute of Physics, Chinese Academy of Sciences, Beijing, China. [4]Yangtze River Delta Physics Research Center Co. Ltd., Liyang, China. [5]Present address: Department of Materials Science and Engineering, Stanford University, Stanford, CA, USA. [6]These authors contributed equally: Zhao Chen, Yuqi Li. ✉e-mail: fxie@iphy.ac.cn; yshu@iphy.ac.cn

can mitigate the volume expansion, reduce strain accumulation and optimize the solid electrolyte interphase (SEI), thus enhancing the cycling stability. It is also evidenced that the dead particles can be efficiently recovered by optimizing the charging/discharging protocols, which have been attracting increasing attention[27–29]. Nevertheless, these approaches would more or less introduce trade-offs such as sacrificed capacity, low initial Coulombic efficiency (ICE) and complex synthesis processes. Although some of these strategies have been successfully verified for alloy anodes such as Si in practical Li-ion batteries (LIBs), the heavier Na^+ ions as well as the larger volume expansion of Sn (420%) than that of Si (280%) bring more severe challenge for NIBs. How to use a simple method to make the alloy-based anode undergo sufficient sodiation/desodiation to exert its capacity and meanwhile provides robust support for the particles to prevent them from electrical isolation during the morphological and structural evolution is of great importance to balance the high capacity and long cycle life. Constructing conductive confining networks during the electrode fabrication (for example, assisted by carbon nanotubes[30–33] and so on) is benefit from relatively easy production. Current studies can mostly achieve the optimization of the alloy anodes at the gram level and obtained improved electrochemical stability in coin-type cells, while it is urgent to understand the performance tailoring mechanism and put step forward the scalable, stable and high-loading Sn anodes towards practical high-energy Ah-level NIBs.

Herein, by leveraging the strong adsorption between single-walled carbon nanotubes (SWCNTs) and crystal plane of micrometre Sn, the constructed cross-linked networks can effectively confine the Sn particles, promoting the superior specific Na storage capacity of 789.4 mAh g^{-1} and 87.6% capacity retention after 6,000 cycles at 2 A g^{-1}. Profiting from the excellent mechanical stability without particle agglomeration, the Sn anode can be scaled up to kilogram level with a high active material ratio of 92%. The assembled Ah-level NIB delivers ~75% capacity retention after 600 cycles between 1.5 V and 3.8 V as well as high volumetric and mass energy density over 435 Wh l^{-1} and 200 Wh kg^{-1} between 1 V and 4.1 V, respectively. The low-temperature performance of the Sn-based pouch cell also surpasses the commercial $LiFePO_4$/graphite battery. Combining the structural characterization with computational study and machine learning with statistical analysis, the superior performance and stability of the micrometre Sn anodes are contributed from adequate topological morphological evolution of the Sn particles with high active material utilization during the cycling owing to the robust support and sustained electrical connectivity from the optimized conductive three-dimensional (3D) networks (Fig. 1). This study provides insight into the role of topological morphological evolution in alloy-based anode particles and presents an effective, scalable strategy to stabilize these anodes using supporting conductive networks, advancing practical applications of next-generation high-energy NIBs.

Building cross-linked networks within micrometre Sn particles

The micrometre Sn was selected for this study considering its smaller surface area, higher compacted density and lower cost[34,35] compared with the nano-sized Sn. The particle size and basic structures of the pristine Sn powders are shown in Supplementary Fig. 1. Since the discovery by Iijima in 1991[36,37], CNTs with excellent mechanical and electrical properties[38–40] can bring high areal loading, improved dynamics and enhanced cycling stability for electrodes[18,30,41]. Therefore, the anode was fabricated with 92 wt% micrometre Sn, 2% SWCNTs (Supplementary Fig. 2) and 6% carboxymethyl cellulose (CMC) binder (9226-SWCNT). Compared with the anode using conventional acetylene black (9226-AB) in Fig. 2a, the Sn particles can be well encapsulated by the SWCNT networks (Fig. 2b,c and Supplementary Fig. 3).

Because of the low Mohs hardness of 1.5 for Sn (ref. 42), cold welding occurs commonly under external forces[43] during the electrode slurry stirring, causing micrometre Sn particles to agglomerate into larger sizes when using conventional conductive carbon such as AB (Fig. 2d, and Supplementary Figs. 4 and 5a,d,g,i,k), which is one of the biggest problems of the unsatisfactory performance of Sn anode. Even if the ratio of AB increases to 20 wt% while that of Sn decreases to 70 wt% (721-AB), such agglomeration is still unavoidable (Supplementary Fig. 5b,e). However, previous studies have shown that process control agents (PCAs) adsorbed on the surface of particles can effectively lower the surface tension and minimize the cold welding[44]. The SWCNTs can act as PCA (Supplementary Fig. 4a) to effectively impede the agglomeration (Fig. 2e and Supplementary Fig. 5c,f,h,j,l). The high-resolution transmission electron microscopy (HRTEM) images of the initial electrodes also verify this finding, which is shown in Supplementary Fig. 6.

To clarify the effect of SWCNTs as PCA to inhibit the agglomeration of Sn particles, the first-principle calculation was performed. On the basis of the β-Sn surface energy data[45,46] and the Gibbs–Wulff crystal growth law[47] reported by Sellers et al. and Eckold et al., we constructed an equilibrium Wulff crystal structure of the Sn electrode (Fig. 2f), and the occupancy of the individual exposed crystal planes was calculated (Supplementary Table 1). Subsequently, we built a model of the Sn electrode surface structure (Supplementary Fig. 7a) centred around the (211) plane, which has the highest exposure percentage at 79.53%. We then carried out structural optimization using selective dynamics. The optimized Sn particle surface structure model was used to study the adsorption of the foreign Sn atom and the SWCNT (Supplementary Fig. 7b). As shown in Fig. 2g,h, it is revealed that the SWCNTs reduce more system energy (0.778 eV/N_{bonds}) than foreign Sn atoms (0.011 eV/N_{bonds}), suggesting that SWCNTs are more likely to adsorb onto the Sn particle, preventing the adsorption of foreign Sn atoms and subsequently inhibiting the agglomeration. Remarkably, unlike the formation of a large number of dislocations inside the micrometre Sn particles of 9226-AB, the SWCNTs in 9226-SWCNT can well cross-link with the CMC binder, uniformly encapsulating the micrometre Sn particles and serving as a protective layer on the micrometre Sn surface, as proved by the Fourier transform infrared (FT-IR) spectra[48,49], scanning electron microscope (SEM), TEM and scanning transmission electron microscope (STEM) images (Supplementary Figs. 8–11). Besides, all the Sn anodes were subjected to 180° peeling tests, and the 9226-SWCNT is able to withstand higher peeling strength (Fig. 2i and Supplementary Fig. 12), which indicates that the cross-linked networks can also provide high mechanical stability of the 9226-SWCNT.

Superior stability of 9226-SWCNT ensured by the cross-linked networks

After the construction of homogeneous and mechanically stable electrodes by SWCNT cross-linked networks, the electrodes were assembled into half cells to further evaluate the electrochemical properties. The 9226-SWCNT demonstrated the highest capacity of 789.4 mAh g^{-1} with an impressive ICE of 89.5% at 0.1 A g^{-1} and the best rate capability of 766.0 mAh g^{-1} at 2 A g^{-1} (Fig. 3a,b). By contrast, 9226-AB exhibited a lower capacity of only 123.7 mAh g^{-1} with an ICE of 14.4% at 0.1 A g^{-1}, while the rate performance is miserable. The 721-AB also shows unsatisfied capacity of 550.2 mAh g^{-1} with an ICE of 80.8% at 0.1 A g^{-1} and 430.7 mAh g^{-1} at 2 A g^{-1}. As shown in Fig. 3c, 9226-SWCNT also exhibits remarkable specific capacity of 654.5 mAh g^{-1} after 6,000 cycles at a current density of 2 A g^{-1}, corresponding to an impressive capacity retention of 87.6%. By contrast, 9226-AB shows ignorable reversible capacity, while the 721-AB still delivers much lower capacity than 9226-SWCNT and requires an activation process of nearly 150 cycles with a sudden capacity drop after 500 cycles (Fig. 3c). Notably, the ratio among the active material, the conductive carbon and the binder of 7:2:1 is commonly used in recent studies for the Sn anode[18,21,50,51], and such low content of active material will cause decreased energy density. Insufficient conductive carbon additives (such as 9226-AB) usually lead to

https://doi.org/10.1038/s41560-026-01974-2

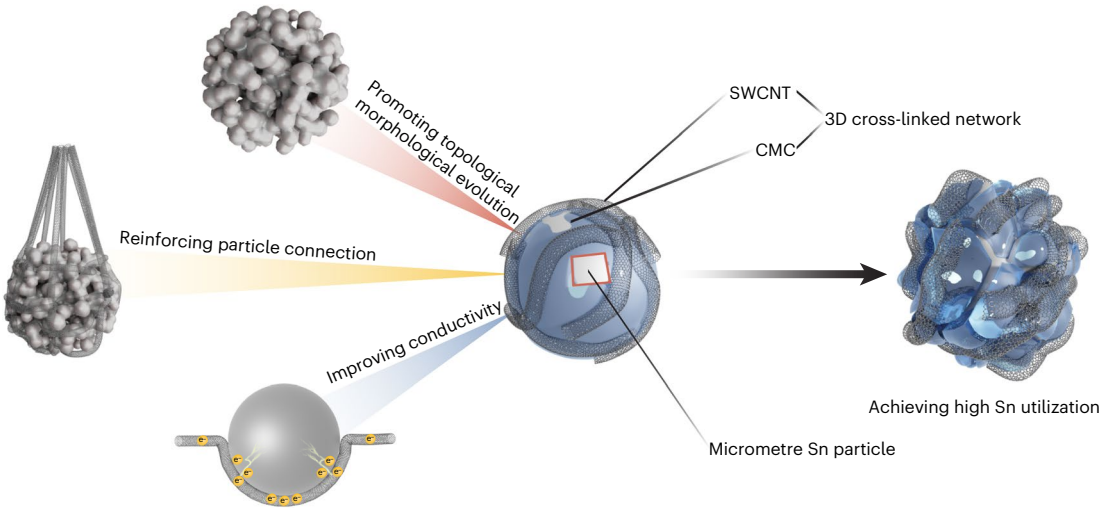

Fig. 1 | The SWCNT-incorporated micrometre Sn anode with the cross-linked networks. The network reinforces the adequate topological morphological evolution and maintains continuous mechanical and electrical connections among Sn particles during cycling. The central image illustrates that the SWCNT cross-linked network uniformly encapsulates the micrometre Sn particle. The three images on the left respectively indicate that the SWCNT network (i) promotes the topological morphological evolution of Sn particles, (ii) mechanically reinforces the particles to maintain reliable electrical contact and (iii) enhances electronic conductivity. The right image shows that micrometre Sn particle undergoes pronounced morphological evolution upon repeated cycling, during which the SWCNT network achieves high Sn utilization.

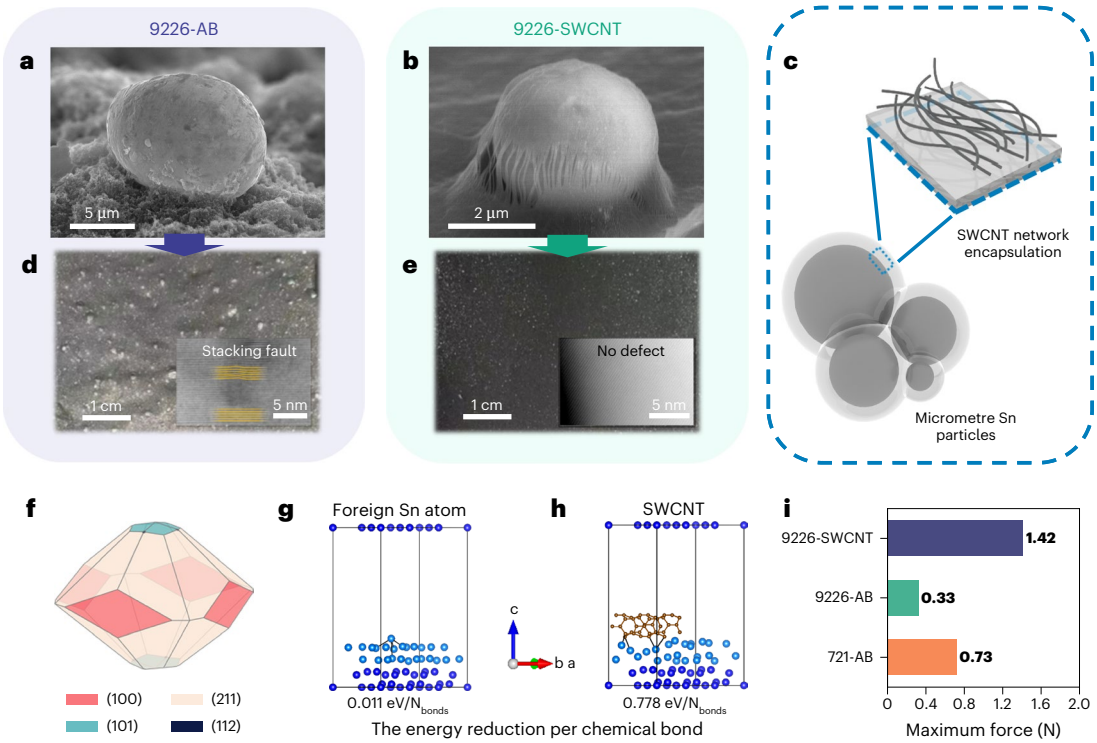

Fig. 2 | Formation and protection of the SWCNT cross-linked networks on micrometre Sn particles. a,**b**, SEM images of the micrometre Sn particles in 9226-AB (**a**) and 9226-SWCNT (**b**) pristine electrodes. **c**, Schematic diagram of the SWCNT network encapsulating micrometre Sn particles. **d**,**e**, Photographs of 9226-AB (**d**) and 9226-SWCNT (**e**) pristine electrodes. The large reflective dots represent the agglomeration of Sn particles, and the surface of 9226-SWCNT is smoother with less agglomeration than 9226-AB. The inset in **d** shows annular bright-field-scanning transmission electron microscopy (STEM) images for 9226-AB. The yellow lines inside represent atomic layers. Stacking fault can be seen in several atomic layers in the centre of the figure. The inset in **e** shows high-angle annular dark-field STEM image for 9226-SWCNT. **f**, The equilibrium Wulff shape of the Sn crystal particle obtained based on surface energy calculations. **g**,**h**, The adsorption scenarios of the foreign Sn atom (**g**) and SWCNT (**h**). The chemical bonds are represented in black. Surface energy reduction values are labelled at the bottom of the graph. **i**, The peel strength of 9226-AB, 721-AB and 9226-SWCNT pristine electrode measures by 180° peel testing.

inferior capacity with inferior rate and cycling performance owing to the poor electronic conductivity (Supplementary Fig. 13). However, SWCNTs well solved this dilemma. The advance of SWCNT is further confirmed by comparing it with other popular conductive agents as shown in Supplementary Fig. 14. Compared with other studies of Sn-based anode for NIBs, 9226-SWCNT achieves the most robust electrochemical performance so far, exhibiting remarkably high current density, high specific capacity and extraordinary cycling life (Supplementary Fig. 15

https://doi.org/10.1038/s41560-026-01974-2

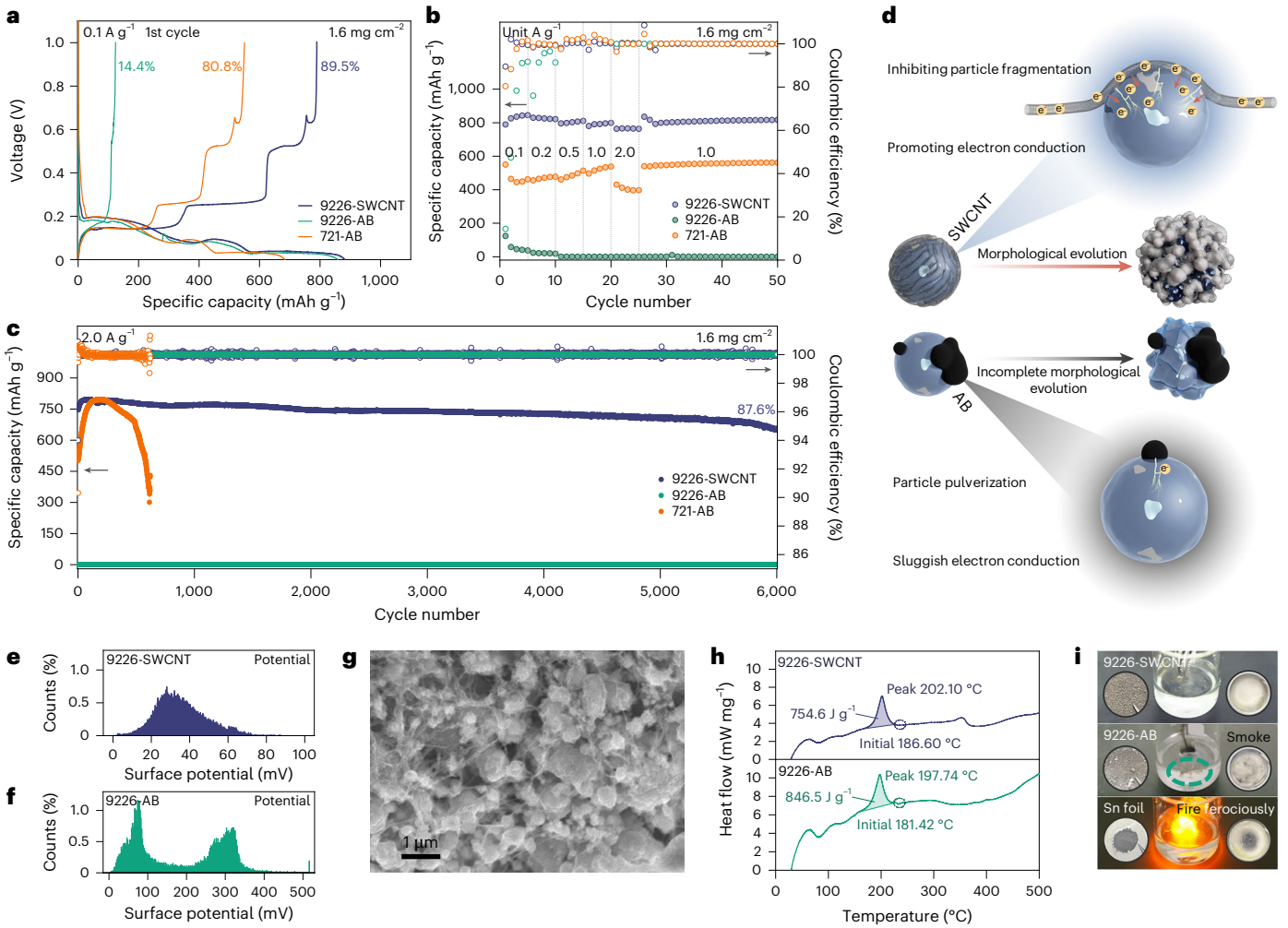

Fig. 3 | Electrochemical and thermal performance of micrometre Sn electrode. **a**, Galvanostatic initial discharge/charge curves of all samples at a current density of 0.1 A g^{-1}. **b**, Rate capability of all samples from 0.1 A g^{-1} to 2.0 A g^{-1}. **c**, Cycling performance of 9226-SWCNT, 9226-AB and 721-AB at a current density of 2.0 A g^{-1}. **d**, Schematic diagram of different effects of SWCNT and AB on the Sn particles. **e**,**f**, Quantitative analysis of potential value distribution on the surface. The root mean square roughness R_q of the surface potential of 9226-SWCNT (**e**) and 9226-AB (**f**) is 0.0125 V and 0.0930 V, respectively. **g**, The SEM image of 9226-SWCNT electrode after 200 cycles. **h**, DSC profiles of the sodiated 9226-SWCNT and 9226-AB after the first discharge process. **i**, Water soaking safety test for sodiated electrodes. The real photos of the corresponding sodiated electrodes and separators are on the left and right side, respectively. The green dashed line indicates the reaction products of 9226-AB with water.

and Supplementary Table 2). Notably, under the assistance of SWCNT cross-linked networks, the mass loading of the micrometre Sn anode can reach maximum 13.4 mg cm^{-2}, corresponding to a high areal capacity of 9.9 mAh cm^{-2} (Supplementary Fig. 16 and Supplementary Table 3).

The different effects of SWCNT and AB on the electrochemical stability of the Sn anodes are illustrated in Fig. 3d. It is also noteworthy that the failure of AB to uniformly wrap Sn particles results in the contact mode between the two parts that is dominated by point contact (Supplementary Fig. 17a–f). In comparison, spontaneously adsorbing of SWCNTs on micrometre Sn particles (Fig. 2f,g) ensures dense face contact and efficient electrical connection[52] in the SWCNT among Sn particles (Supplementary Fig. 11). Except for the difference between intrinsic conductivity of SWCNT and AB, the conductivity of face contact is much better than that of point contact (Supplementary Fig. 17g). The improvement in electrical connection is also accompanied by the homogenization of the electric field distribution[53] as proved by Kelvin probe force microscopy (Fig. 3e,f and Supplementary Fig. 18), which accelerates the directional shuttle of Na^+ ions. Accordingly, the morphological evolution process of micrometre Sn is ultimately different. The 9226-SWCNT electrode accelerates the evolution of the particles towards coral-like morphology, leading to the highest capacity and continuous electrical connection during the cycling (Supplementary Fig. 19a–c). By contrast, the micrometre Sn particles with AB remain dense chunks and aggregate to lose connection among each other (Supplementary Fig. 19d,e). X-ray micro-computed tomography (μ-CT) further demonstrates that a majority of micrometre Sn active particles in 9226-SWCNT undergo morphological transformation during cycling, transforming from dense spheres (bright region) to porous coral-like structures (dark region) as shown in Supplementary Fig. 20. Such coral-like morphology can also facilitate better kinetics owing to the porous structures and larger surface area that leads to better electrolyte wettability (Supplementary Fig. 21) and more Na^+ ion diffusion channels, represented by the higher ionic conductivity with the average diffusion coefficient of Na^+ ions in 9226-SWCNT than both 9226-AB and 721-AB (Supplementary Fig. 22). This was also verified by the electrochemical impedance spectroscopy (EIS) and cyclic voltammetry results so that lower impedance and higher reversibility could be obtained in 9226-SWCNT (Supplementary Figs. 23–25).

Although the Sn anode in ether-based electrolytes does not suffer from particle pulverization as in ester-based electrolyte[54] (Supplementary Fig. 26), one of the intrinsic reasons of capacity decay

https://doi.org/10.1038/s41560-026-01974-2

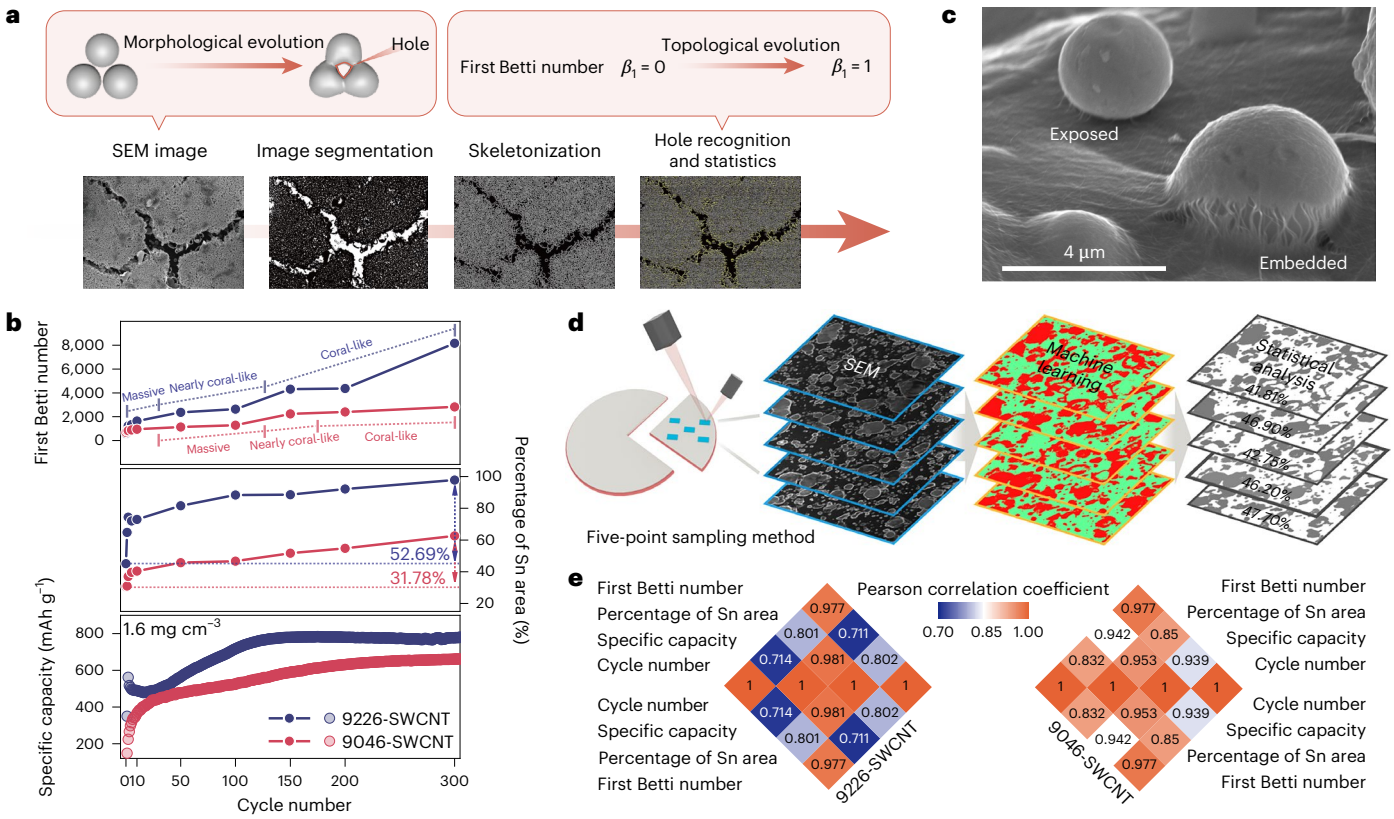

Fig. 4 | Topological morphological evolution and exposure effect. a, Scheme of topological structure analysis of micrometre Sn particles. **b**, Plot of degree of topological evolution (expressed as the β_1) versus degree of exposure effect (expressed as the area percentage of the exposed Sn) and the specific capacity of micrometre Sn particles cross-linked with 2%/4% SWCNTs in NIBs under 2 A g^{-1} cycling. **c**, The cross-section SEM image of a micrometre Sn particle representing the exposure effect under SWCNT cross-linked network encapsulation. **d**, Scheme of the exposure effect study of micrometre Sn particles through machine learning. **e**, Pearson correlation coefficients among various cycle number, specific capacity, area percentage of exposed Sn and β_1 of 9226-SWCNT and 9046-SWCNT. The Pearson correlation coefficient is an index for linear relationships. The values lie between −1 (perfect negative) and 1 (perfect positive), with 0 signifying uncorrelated data. Each number in the grid represents the Pearson correlation coefficient between particular two variables.

for the Sn-based anodes is the loss of electrical connection among the whole active particles during cycling, so that the deactivated Sn or 'dead Sn' forms and the ratio of active Sn decreases (Supplementary Fig. 27), resulting in the reduction of Sn utilization. The SWCNTs functioned as a mesh[31] to encapsulate the active micrometre Sn particles, forming 3D conductive matrix (Fig. 3g). In addition, this 3D network also provides anchoring of the micrometre Sn particles, promising the 9226-SWCNT with no detachment after cycling (Supplementary Fig. 28).

The interface of the Sn-based anodes was also investigated via X-ray photoelectron spectroscopy (XPS) for 9226-SWCNT and 721-AB (9226-AB is excluded from comparison owing to its poor electrochemical performance). The F 1*s* spectra in 9226-SWCNT reveal a higher content of NaF, especially on the surface layer (Supplementary Fig. 29a,b). Conversely, 721-AB has only a few amounts of NaF at inner layers but almost no NaF at the surface layer instead of dominating by P–F bonds. The C 1*s* spectrum[22] of 9226-SWCNT reveals a lower content of Na_2CO_3 but a higher content of organic species at both the surface and inner layers of the SEI, which is opposite to 721-AB (Supplementary Fig. 29c,d). The ideal combination of the SEI in 9226-SWCNT dominated by NaF and organic components[55] with trace amounts of unstable Na_2CO_3 provides exceptional flexibility and strength, making it highly suitable for Sn-based anode stable cycling.

In addition to the electrochemical stability, the fully sodiated 9226-SWCNT also demonstrates enhanced thermal stability compared with 9226-AB, as evidenced by its higher decomposition temperature and reduced exothermic behaviour (Fig. 3h and Supplementary Fig. 30). It is also found that the sodiated 9226-SWCNT has the gentlest reaction without any smoke and fire when soaked in the water compared with 9226-AB and pure Sn foil (Fig. 3i and Supplementary Note 1).

In short, the superior performance and stability of 9226-SWCNT can be attributed to the established 3D conductive matrix and cross-linked networks by the assistance of SWCNTs. These ensures the optimized morphology and interface evolution, uniformed electric field distribution, higher Na^+ ion kinetics and continuous electrical connection among Sn particles, which maintains always adequate Sn utilization during the whole lifespan.

Topological morphological evolution of the Sn particles during cycling

Considering the superior advantages of SWCNTs, the effect of different SWCNT contents on the electrochemical properties was investigated. It is expected that using 0.2 wt% and 0.6 wt% SWCNTs (SWCNTs and AB were mixed together into the anodes to keep the total ratio of the conductive carbons at 2 wt%) led to inferior capacity especially at high current densities (Supplementary Fig. 31). However, albeit similar reversible capacities are delivered at a low current density of 0.1 A g^{-1}, the Sn anode with an increased SWCNT ratio to 4 wt% (9046-SWCNT) shows deteriorated rate and cycling performance (Supplementary Fig. 31b,c). This suggests that the electrochemical performance of Sn-based anode cannot be solely dependent on the electrical conductivity by mixing more conductive additives.

Taking into account the 9226-SWCNT and 721-AB, their capacity difference is strongly influenced by the coral-like morphological evolution induced by repeated sodiation/desodiation with volumetric

'expansion–contraction' during cycling, which represents the Sn utilization. Therefore, the coral-like morphological evolution was quantitatively investigated to verify its effect on the electrochemical performance of 9226-SWCNT and 9046-SWCNT. As illustrated in Fig. 4a, the formed holes during the evolution of coral-like morphology can be interpreted as a topological behaviour, quantified by the first Betti number (β_1)[56], which serves as an indicator of the total number of closed holes. Higher β_1 represents more thorough topological morphological evolution. To facilitate the determination of β_1, skeletonized topological equivalence analysis[57,58] was performed on SEM images at various cycling stages. As depicted in Fig. 4b and Supplementary Figs. 32–34, 9226-SWCNT has higher β_1 than 9046-SWCNT during the cycling, indicating a more adequate topological structure and faster evolutionary process. These factors account for their observed capacity difference during cycling.

Why does 9046-SWCNT, despite its higher SWCNT ratio, fail to undergo adequate topological morphological evolution and achieve effective Sn utilization during the cycling? Initially, the micrometre Sn particles in the electrode are partially embedded and shielded by the SWCNT–CMC cross-linked networks (Fig. 4c and Supplementary Fig. 35). Only the exposed particles efficiently participate in the Na storage process. By contrast, the embedded particles exhibit reduced activity from limited electrolyte contact, resulting in inadequate topological morphological evolution and worse ion diffusion ability compared with 9226-SWCNT (Supplementary Figs. 21, 36 and 37). The conversion from the embedded to exposed Sn, driven by the sodiation-induced expansion during the cycling, is also necessary to provide more active Sn for the Na storage process to ensure high utilization of active material. Notably, the capacity disparity caused by exposure effect even cannot be fully eliminated through the low-rate activation process (Supplementary Fig. 38).

To verify the above hypothesis, we captured the SEM images of the Sn anodes at desodiated status after 300 cycles. By manually pre-labelling a small number of regions as demonstration, the exposed Sn and substrate regions of the electrodes in all SEM images were distinguished by machine learning[59] as shown in Fig. 4d. The percentage of the area occupied by exposed Sn can be obtained by statistical analysis (Supplementary Figs. 39–41). It is found that the area percentage of exposed Sn for 9226-SWCNT is higher than that of 9046-SWCNT, and the increasing rate of the area percentage is also higher for the former during the cycling (Fig. 4e), which coincides with the XPS spectrum that the Sn atom ratio of 9226-SWCNT is higher than that of 9046-SWCNT (Supplementary Fig. 42). This means that an optimal SWCNT content ensures more exposed active Sn particles and facilitates the conversion from embedded ones to exposed active species during the cycling, which is analogous to the seed to break out of the ground (Supplementary Fig. 43). The exposure effect is also suitable for the Si anode in LIBs, which will be discussed in Supplementary Note 2.

The Pearson correlation analysis of cycle number, specific capacity, area percentage of exposed Sn, and β_1 of 9226-SWCNT and 9046-SWCNT in the first 300 cycles are shown in Fig. 4e. The values of 0.981 in 9226-SWCNT and 0.953 in 9046-SWCNT demonstrate the strong linear correlation between specific capacity and the area percentage of exposed Sn. Consequently, the lower capacity observed in 9046-SWCNT compared with 9226-SWCNT is attributed to less adequate topological morphological evolution (smaller β_1) and lower area percentage of exposed Sn so that the utilization of active Sn for the Na storage is limited during the cycling, thus leading to lower capacity retention (poorer cycling stability). After an in-depth study of the statistical correlation between the four indicators, β_1, area percentage of exposed Sn, specific capacity and cycle number, respectively, the growth correspondence between each two indicators is constant (Supplementary Fig. 44). In other words, it is possible to predict the specific capacity with the area of exposed Sn particles and their topological morphological evolution of Sn anodes in later cycling.

It is now reasonable to conclude that the superior Na storage performance of 9226-SWCNT can be attributed to the sufficient sodiation/desodiation of the Sn particles with topological morphological evolution during the whole cycling process. The optimized cross-linked networks with proper SWCNT content ensure continuous electrical connectivity among the Sn particles, facilitating efficient electronic transport. Simultaneously, the improved contact between the exposed Sn particles and the electrolyte can promote abundant ionic transport. Moreover, the SWCNT networks can provide robust support to impede the mechanical/electrical isolation of the micrometre Sn particles and the pulverization of the electrode (Supplementary Figs. 26 and 27) during the complete topological morphological evolution, thus keeping the high utilization of active material.

Scaling up the Sn anode for Ah-level NIBs

To evaluate the practical performance of the Sn anodes, 9226-SWCNT was assembled with $Na[Cu_{1/9}Ni_{2/9}Fe_{1/3}Mn_{1/3}]O_2$ cathode to construct coin-type full cells and investigate the electrochemical performance. The initial discharge capacity of the full cell reaches 115.2 mAh g^{-1} (based on cathode) at 20 mA g^{-1} with a high ICE of 82.6% and excellent cycling performance over 350 cycles at 0.2 A g^{-1} with a capacity retention of 82.2% (Supplementary Fig. 45).

To further explore the potential of Sn-based anode for practical applications, the first Ah-level pouch cells using $Na[Cu_{1/9}Ni_{2/9}Fe_{1/3}Mn_{1/3}]O_2$ and 9226-SWCNT were fabricated. During the slurry preparation process, the micrometre Sn particles were well protected by SWCNTs during stirring, without any agglomeration (Fig. 5a and Supplementary Fig. 46). Benefiting from the high compacted density of anode, the pouch cell shows the capacity of 2.7 Ah and achieves high energy density over 200 Wh kg^{-1}/453 Wh l^{-1} and 190 Wh kg^{-1}/430 Wh l^{-1} (Fig. 5b and Supplementary Fig. 47) between 1 V and 4.1 V under the current of 0.1 A and 0.3 A, respectively, much superior than that of 150 Wh kg^{-1}/256 Wh l^{-1} (volumetric energy density boosted by 76%) for the pouch cells based on hard carbon anode (Supplementary Fig. 48), which is in the leading position among reported Ah-level NIBs, even surpassing the $LiFePO_4$/graphite commercial LIBs (Supplementary Fig. 49 and Supplementary Table 4). It is also shown in Fig. 5c that the pouch cell with 9226-SWCNT anode maintains nearly 75% of its capacity after 600 cycles at a current of 8 A (~15 min charge, 4 C) between 1.5 V and 3.8 V. The energy densities of the cell can still achieve 134 Wh kg^{-1} and 303 Wh l^{-1} under such high rate. By contrast, the commercial $LiFePO_4$/graphite Ah-level cell exhibited a capacity retention of only 32% after 600 cycles (Supplementary Fig. 50). The Sn-based cell also exhibits superior low-temperature performance to that of the commercial $LiFePO_4$/graphite cell. The discharge capacity retention at −20 °C (charged at room temperature) can be 65.6%, which is much higher than 47.6% for the $LiFePO_4$ system. When charged and discharged both at −20 °C, the Sn-based cell can still deliver 61.2% of its room-temperature capacity with stable cycling, while the $LiFePO_4$-based cell shows almost no performance (Fig. 5d,e, Supplementary Fig. 51 and Supplementary Table 5). These results indicate the feasibility of the scale-up of the 9226-SWCNT electrode and the application in Ah-level cells, promising the great potential of next-generation high-energy NIBs using alloy-based anode.

Conclusion

In summary, assisted by the incorporation of SWCNTs, we have demonstrated a scalable, stable and high-loading micrometre Sn anode with a high active material ratio of 92 wt%. The cross-linked networks formed by the SWCNTs can prevent the loss of electrical connection and provide strong adhesion for the Sn particles during deep topological morphological evolution, which guarantees the high capacity delivery of the Sn anode with superior mechanical, thermal and electrochemical stability. This anode achieves a high reversible specific capacity and impressive cycling stability over 6,000 cycles at a current

https://doi.org/10.1038/s41560-026-01974-2

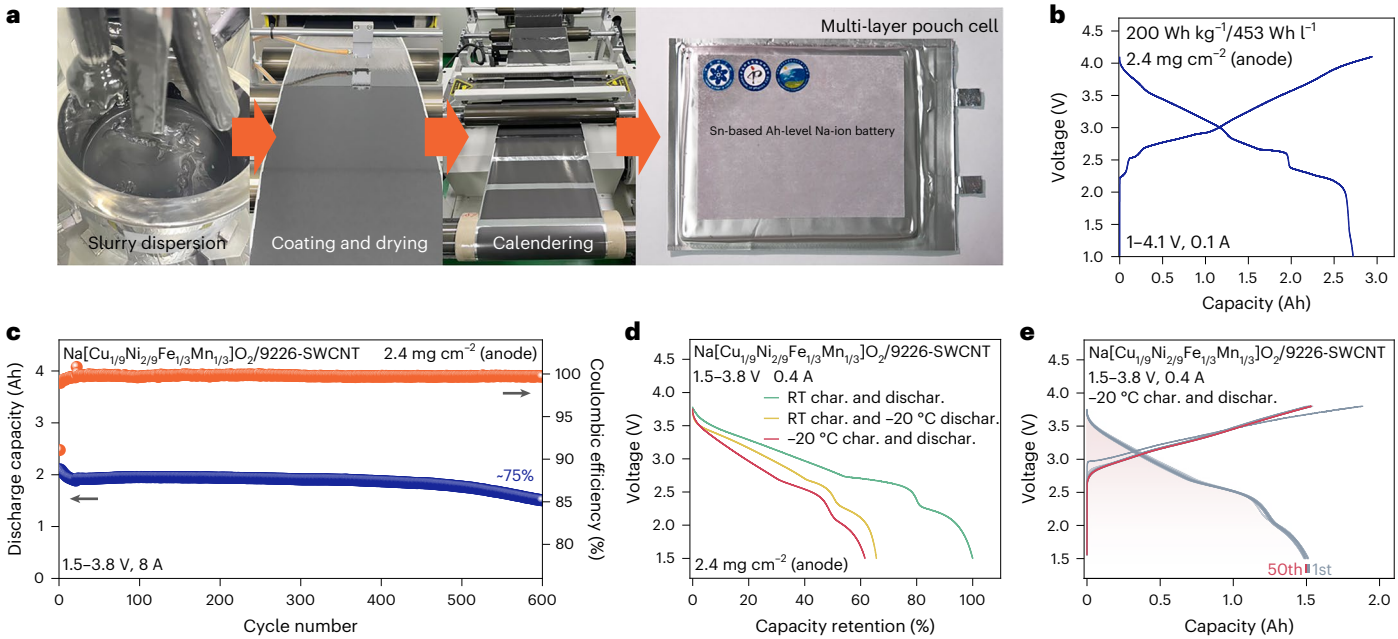

Fig. 5 | Practical performances of the prepared micrometre Sn anode in Ah-level NIBs. a, The real photos of the Ah-level pouch cell production process. Slurry dispersion, coating, drying and calendering process of 9226-SWCNT electrode and Sn-based multi-layer NIB pouch cell. **b**,**c**, The electrochemical performance of the $Na[Cu_{1/9}Ni_{2/9}Fe_{1/3}Mn_{1/3}]O_2$/9226-SWCNT Ah-level pouch cell. Galvanostatic charge/discharge curve of the pouch cell at a current of 0.1 A between 1 V and 4.1 V (**b**). Cyclic capability of the $Na[Cu_{1/9}Ni_{2/9}Fe_{1/3}Mn_{1/3}]O_2$/9226-SWCNT pouch cell at a current of 8 A between 1.5 V and 3.8 V (**c**). **d**,**e**, Low-temperature performance of the $Na[Cu_{1/9}Ni_{2/9}Fe_{1/3}Mn_{1/3}]O_2$/9226-SWCNT NIB pouch cell. RT represents room temperature, while char. and dischar. represent charge and discharge, respectively. Comparison of discharge curves at 0.4 A under different temperature conditions (**d**). Charge–discharge curves of $Na[Cu_{1/9}Ni_{2/9}Fe_{1/3}Mn_{1/3}]O_2$/9226-SWCNT Ah-level cells over the first 50 cycles at −20 °C (**e**).

density of 2 A g^{-1}. The Sn-based Ah-level NIB pouch cell with Cu-based cathode delivers 2.7 Ah capacity and exceptional volumetric energy densities over 453 Wh l^{-1} between 1 V and 4.1 V with nearly 75% capacity retention after 600 cycles between 1.5 V and 3.8 V at a high rate of 4 C. The low-temperature performance of the Sn-based pouch cell is also superior to that of the $LiFePO_4$/graphite cell. This work offers important insight into achieving excellent capacity, rate capability and cycling stability in practical alloy-based anodes by ensuring high active material utilization via continuous and adequate topological morphological evolution that is supported by robust mechanical and electrical connections. These findings highlight the great potential of next-generation high-energy NIBs.

Methods

Electrochemical preparation and electrochemical measurements

For anode materials of coin-type cell, the commercial pure micrometre Sn powders (Sigma-Aldrich, 99.80%) and carbon-based conductive additive materials SWCNT (Tuball, OCSiAl) or AB (Alfa Aesar) are dispersed into water using sodium CMC (Grade 2200, Daicel) as binders (mass ratio of micrometre Sn:SWCNT:CMC = 92:2:6 and 90:4:6, Sn:SWCNT:AB:CMC = 92:0.2:1.8:6 and 92:0.6:1.4:6 or micrometre Sn:AB:CMC = 92:2:6 and 70:20:10 coating on Al foil). The layered O3-type cathode (mass ratio of $Na[Cu_{1/9}Ni_{2/9}Fe_{1/3}Mn_{1/3}]O_2$:AB:PVDF = 93.5:3.5:3 coating on Al foil) was provided by HiNa Battery Technology. The electrolyte is 1 M (mol l^{-1}) $NaPF_6$ (Kishida Chemical, 99%) dissolved in diethylene glycol dimethyl ether (Sigma-Aldrich, 99.5%), labelled as 1-G2.

Coin cells (CR2032) were assembled inside a glovebox under the Ar environment. The electrolyte volume for each cell was fixed at 100 µl. The composite separator consisting of a Whatman GF/A glass fibre layer and Celgard 3501 polypropylene nanoporous membrane was used throughout this work. Pristine Sn-based electrode was punched into discs with a diameter of 10 mm. The Na ingot (99.8%, Alfa) was rolled into Na foil and cut into pieces as the counter electrodes with a diameter of 12 mm. The half cell was prepared using pure Na metal foil as a counter electrode, and pristine Sn-based electrode as the anode. The loading masses of the Sn-based electrodes for half cells were 1.6 mg cm^{-2}, 2.4 mg cm^{-2}, 3.4 mg cm^{-2}, 5.0 mg cm^{-2}, 8.3 mg cm^{-2} and 13.4 mg cm^{-2}, respectively. The full cells were prepared using $Na[Cu_{1/9}Ni_{2/9}Fe_{1/3}Mn_{1/3}]O_2$ as the cathode and 9226-SWCNT as the anode. The diameters of cathode and anode for full cell are both 10 mm, and the corresponding negative/positive (N/P) ratio was controlled at about 1.05. 1-G2 was used as the electrolyte for both half cells and full cells. The current densities used for electrochemical testing in half cells are 0.1 A g^{-1}, 0.2 A g^{-1}, 0.5 A g^{-1}, 1.0 A g^{-1} and 2.0 A g^{-1}, respectively, based on the mass of Sn anodes. Note that the small-current pre-activation process at 0.2 A g^{-1} before the cycling test is not shown in Fig. 3c. In the coin-type full cells, the areal loadings are 1.6 mg cm^{-2} (anode) and 10.0 mg cm^{-2} (cathode), while the current densities are 20 mA g^{-1} and 0.2 A g^{-1}, respectively, based on the mass of cathode. Note that the small-current pre-activation process at 20 mA g^{-1} before the cycling test is not shown in Supplementary Fig. 45b. For Si-based anode materials, the commercial pure micrometre Si powders (Zhongye, 99.90%) and SWCNT are dispersed into water using sodium CMC (Grade 2200, Daicel) as binders (mass ratio of micrometre Si:SWCNT:CMC = 85:6:9 and 70:12:18).

The operation temperature of all cells is ambient temperature (~35 °C). Galvanostatic charge–discharge measurements of all coin-type cells were carried out using the NEWARE battery testing system (CT-4008Tn-5V10mA-164). EIS test was performed on an IM6e Zahner electrochemical workstation over a frequency range from 1 MHz to 100 mHz. Ex situ EIS curves of each half cell were recorded when the cells were fully charged, which correspond to the 1st, 50th and 200th cycles between 0 V and 1 V at a current density of 2 A g^{-1}. Cyclic voltammetry curves were recorded by an Autolab 302 electrochemical

workstation over the initial 3 discharge–charge cycles in the potential range of 0–1 V at scan rates of 0.1 mV s^{-1}, 0.2 mV s^{-1}, 0.5 mV s^{-1}, 1 mV s^{-1}, 1.5 mV s^{-1}, 2 mV s^{-1} and 3 mV s^{-1}.

For the Ah-level pouch cell, the 9226-SWCNT and $Na[Cu_{1/9}Ni_{2/9}Fe_{1/3}Mn_{1/3}]O_2$ were prepared by the coating machine. First, the composition of the anode (mass loading ~2.43 mg cm^{-2}) slurry was 92 wt% commercial pure micrometre Sn powder, 2 wt% SWCNT and 6 wt% CMC. Then, the electrode preparation used extrusion coating on Al foil, followed by drying treatment at ~60 °C and a calendering process under pressure of 5–10 tons. The cathode slurry (total mass loading ~16 mg cm^{-2}) contained 92 wt% active material. It was cast onto Al foil and subsequently dried under vacuum. The corresponding N/P ratio is about 1.05. The electrolytes used for the Ah-level pouch cells are 1-G2. The electrolyte was prepared and dried using molecular sieves (Duoduo Chemical, 4 Å) in a high-purity Ar-filled glovebox. The $LiFePO_4$/graphite batteries provided by Zhuoneng New Energy have nominal specific capacity ~2 Ah.

The Ah-level pouch cells were assembled in a dry room, sealed in Al plastic film and comprised 9226-SWCNT anode, $Na[Cu_{1/9}Ni_{2/9}Fe_{1/3}Mn_{1/3}]O_2$ cathode, Celgard 3501 membrane separator and the 1-G2 electrolyte (2.5 g Ah^{-1}). The cells were operated at ambient temperature (~35 °C). Galvanostatic charge/discharge test was conducted on a NEWARE battery test system (CT-4008Tn-5V12A-S1). The currents used for the electrochemical test are 0.1 A (for Fig. 5b), 0.3 A (for Supplementary Fig. 47), 0.4 A (for Fig. 5d,e) and 8.0 A (for Fig. 5c), respectively. The size of the pouch cell is 79.9 mm × 65.0 mm × 3.3 mm ($L \times W \times H$) before cycling. The low-temperature performance of the Sn-based NIB and commercial $LiFePO_4$/graphite LIB were carried out by charging the cells at room temperature or −20 °C and discharging at −20 °C. The pouch cell was tested under a stabilized stack pressure of ~23 kg during electrochemical cycling. Volumetric energy density is calculated based on the initial cell volume. Note that the activation (formation) process using a smaller current of 0.4 A before the cycling measurement is not shown in Fig. 5c.

Characterization

All electrodes were disassembled from coin-type cells under Ar atmosphere, washed several times with 1,2-dimethoxyethane and dried in an Ar-filled transfer tube for ex situ tests. Powder X-ray diffraction patterns were measured using a Bruker-AXS D8 ADVANCE diffractometer with a Cu Kα radiation source. Morphology and energy-dispersive X-ray spectra were investigated via a Hitachi-S4800 SEM. For acquiring cross-section SEM images, the electrodes were processed using a JOEL IB-19510CP cross-section polisher. Specimens for TEM and SEM observations were prepared using a focused ion beam (FIB; Thermo Scientific Helios 5 CX). Before milling the sample, a Pt protective layer was deposited. As for SEM images, the electrodes were cut into 1/4 disc in Ar atmosphere. Following this, five distinct areas were selected on each electrode using the five-point sampling method to obtain SEM images. SEM images were processed using image region segmentation to differentiate micrometre Sn particles from the surrounding holes. On the basis of the spatial distribution of these holes, the skeletonization[60] of micrometre Sn particle structures was performed in Fiji ImageJ software (version 1.53t) to enable accurate hole counting and determine the first Betti number. The exposed micrometre Sn particles of electrode in SEM images were identified for analysis using machine learning from Trainable Weka Segmentation plug-in in Fiji ImageJ software (version 1.53t). The classifier of machine learning was trained to discriminate the exposed micrometre Sn particles based on specific contrast ranges in the images. The detailed operations can be found in Supplementary Note 3. Then statistics analysis of machine learning was performed to obtain the percentage of exposed micrometre Sn particle area. Pearson correlation coefficient was used to represent the degree of correlation between each two of these factors: cycle number, specific capacity, percentage exposed micrometre Sn/Si particle area and first Betti number. The formula of the Pearson correlation coefficient is shown below:

$$r = \frac{\sum_{i=1}^{n}(X_i - \bar{X})(Y_i - \bar{Y})}{\sqrt{\sum_{i=1}^{n}(X_i - \bar{X})^2}\sqrt{\sum_{i=1}^{n}(Y_i - \bar{Y})^2}} \quad (1)$$

where $\bar{X}$ and $\bar{Y}$ are the average over the X_i and Y_i samples. The fine microstructure was obtained by using HRTEM (JEM 2100 plus). The annular bright-field and high-angle annular dark-field images were performed using a STEM (JEOL ARM-200F) equipped with dual spherical aberration (Cs) correctors for both the condenser and objective lenses. The high-angle annular dark-field detector was operated with an acceptance angle range of 90–370 mrad. Optical microscopic images were captured in a dark-field environment within a glovebox at ambient temperature, using a Leica DM6 metallographic microscope equipped with a charge-coupled device camera. Wettability was assessed using a DataPhysics OCA40 automatic contact angle instrument. To investigate the surface element chemical state, XPS (Thermo Scientific) was used, utilizing an ESCALAB 250 Xi spectrometer with Mg/Al Kα X-ray source. FT-IR spectra were recorded by a Bruker VERTEX 70 V spectrophotometer in attenuated total reflection mode under atmospheric conditions. Differential scanning calorimetry (DSC) was performed using a NETZSCH STA 449F3 thermal analyser, heating samples from room temperature to 500 °C at 10 °C min^{-1} under Ar flow. Surface roughness and charge distribution were investigated with a Bruker Multimode 8 atomic force microscope equipped with the amplitude modulation-Kelvin probe force microscopy module operating in Peak Force Tapping mode. Using a single-pass scanning method, the surface topography and potential pictures of the sample could be obtained simultaneously. The conductive probe was SCM-PIT (0.01–0.025 Ω cm antimony (n) doped Si). The 3D submicrometre-scale structural state of the electrodes was observed by using X-ray μ-CT (nanoVoxel-2000). Operating at a test voltage of 60 kV and a current of 30 μA, this technique provided a spatial resolution of 500 nm. The Bruker Skyscan 1276 with a minimum pixel size of 2.8 μm is also used as a μ-CT for the characterization of the 3D structural state of electrodes. The 180° peel strength test of electrodes was measured using an electronic universal material testing machine (MTS Instron CMT6103) in tensile mode under atmospheric conditions at ambient temperature. The electrodes were fabricated by normal coating and rolling process, and then cutting into rectangular shape with a size of 60 mm × 20 mm. The total mass loading of the electrode for peel strength testing was in the range of 2.2–2.5 mg cm^{-2}. The electrode was stretched at a rate of 10 mm min^{-1} until complete separation of powder and current collector. The force displacement curves were continuously monitored. The electrochemical dilatometry (ECD) was measured by a pressure transducer (Chengying Transducer, HZC-T-200N) under 0.5 A g^{-1}.

Calculations

First-principles computations were carried out using the Vienna Ab initio Simulation Package (VASP, version 5.4.4), in conjunction with the projector augmented-wave approach for density functional theory calculations. The exchange–correlation functional was treated within the Perdew–Burke–Ernzerhof generalized gradient approximation. A plane-wave cut-off energy of 520 eV was used, and Γ-centred Monkhorst–Pack k-point meshes of appropriate density were adopted for Brillouin-zone sampling. Electronic and ionic relaxations were converged to 1×10^{-5} eV (EDIFF) and −0.02 eV $Å^{-1}$ (EDIFFG), respectively.

Bulk β-Sn was modelled in its body-centred tetragonal phase (Supplementary Fig. 52), starting from experimental lattice parameters reported by Sellers et al. Relaxation with a 3 × 3 × 6 k-point grid yielded equilibrium lattice constants of $a = b = 5.880$ Å and $c = 3.172$ Å and an energy of −3.996 eV per Sn atom. This optimized structure

served as the reference for all subsequent modelling. The equilibrium Wulff shape of β-Sn was constructed with pymatgen (v2023.8.10) using surface energies of low-index facets taken from Sellers et al. and Eckold et al. (Supplementary Table 6), and the resulting facet area fractions for the {100}, {101}, {112}, {211}, {301} and {321} families are summarized in Supplementary Table 1. All crystal structures were visualized with VESTA (v3.4.3).

To describe the Sn electrode surface, a β-Sn(211) slab was generated from the optimized bulk structure using the Atomic Simulation Environment (ASE, v3.25.0). As shown in Supplementary Fig. 7a, the slab cell parameters were set to a = 8.683 Å, b = 20.156 Å and c = 26.191 Å, exposing the (211) surface with sufficient vacuum along the surface normal. During structural optimization (3 × 1 × 1 k-point mesh), the bottom two Sn layers were fixed to mimic bulk behaviour, while the top two layers were fully relaxed; the optimized geometry is presented in Supplementary Fig. 7b.

To elucidate the mechanism by which SWCNTs suppress Sn agglomeration, as schematically illustrated in Fig. 2f,g, four models were constructed on the basis of the β-Sn(211) surface: (i) a Sn adatom (Supplementary Fig. 7c), (ii) an isolated SWCNT (Supplementary Fig. 7d), (iii) a Sn adatom adsorbed on the Sn(211) surface (Supplementary Fig. 7e) and (iv) an SWCNT adsorbed on the Sn(211) surface (Supplementary Fig. 7f). The (6,0) SWCNT segment was generated with ASE and then aligned and merged with the surface slab in VESTA, while keeping the cell dimensions at a = 8.683 Å, b = 20.156 Å and c = 26.191 Å. In all adsorption calculations, the cell vectors and the bottom two Sn layers were fixed, and the top two Sn layers together with all adsorbate atoms were relaxed using a 3 × 1 × 1 k-point mesh.

To quantify the interaction strength of Sn adatoms and SWCNTs with the Sn surface, Sn–Sn and Sn–C bonds were identified based on interatomic distances relative to the sum of covalent radii (r_{Sn} = 1.41 Å, r_C = 0.77 Å). Pairs within 100–120% of the summed covalent radii were counted as chemical bonds, giving nominal bond-length thresholds of ~2.82 Å for Sn(surface)–Sn(adatom) and ~2.18 Å for Sn(surface)–C(SWCNT). For each model, the total energy reduction upon adsorption was divided by the number of such bonds to obtain an average stabilization energy per bond; the corresponding energies and bonding statistics are summarized in Supplementary Table 7.

Model construction, data post-processing and automatic monitoring of VASP convergence were carried out with in-house Python scripts (Python 3.9.6, 64-bit). In particular, ionic convergence was verified by parsing OUTCAR files and checking for the 'reached required accuracy' message. The full input scripts used to generate the Wulff shape, surface slabs, SWCNT models and convergence checks are provided in Supplementary Note 4.

Data availability

The data supporting the findings of this study are available within the article and its Supplementary Information files.

References

1. Wu, X. et al. Tin-based anode materials for stable sodium storage: progress and perspective. *Adv. Mater.* **34**, e2106895 (2022).
2. Lao, M. et al. Alloy-based anode materials toward advanced sodium-ion batteries. *Adv. Mater.* **29**, 1700622 (2017).
3. Winter, M. & Besenhard, J. Electrochemical lithiation of tin and tin-based intermetallics and composites. *Electrochim. Acta* **45**, 31–50 (1999).
4. Wang, C., Wang, L., Li, F., Cheng, F. & Chen, J. Bulk bismuth as a high-capacity and ultralong cycle-life anode for sodium-ion batteries by coupling with glyme-based electrolytes. *Adv. Mater.* **29**, 1702212 (2017).
5. Li, W. et al. Layered phosphorus-like GeP5: a promising anode candidate with high initial coulombic efficiency and large capacity for lithium ion batteries. *Energy Environ. Sci.* **8**, 3629–3636 (2015).
6. Zhang, L., Wu, H. B., Liu, B. & Lou, X. W. Formation of porous SnO_2 microboxes via selective leaching for highly reversible lithium storage. *Energy Environ. Sci.* **7**, 1013–1017 (2014).
7. Fukunishi, M. et al. Optimizing micrometer-sized Sn powder composite electrodes for sodium-ion batteries. *Electrochemistry* **87**, 70–77 (2019).
8. Kravchyk, K. et al. Monodisperse and inorganically capped Sn and Sn/SnO_2 nanocrystals for high-performance Li-ion battery anodes. *JACS* **135**, 4199–4202 (2013).
9. Chan, C. K. et al. High-performance lithium battery anodes using silicon nanowires. *Nat. Nanotechnol.* **3**, 31–35 (2008).
10. An, W. et al. Scalable synthesis of ant-nest-like bulk porous silicon for high-performance lithium-ion battery anodes. *Nat. Commun.* **10**, 1447 (2019).
11. Wang, L. et al. 3D porous tin created by tuning the redox potential acts as an advanced electrode for sodium-ion batteries. *ChemSusChem* **11**, 3376–3381 (2018).
12. Liu, Z., Yu, X.-Y., Lou, X. W. & Paik, U. Sb@C coaxial nanotubes as a superior long-life and high-rate anode for sodium ion batteries. *Energy Environ. Sci.* **9**, 2314–2318 (2016).
13. Palaniselvam, T. et al. Sodium storage and electrode dynamics of tin–carbon composite electrodes from bulk precursors for sodium-ion batteries. *Adv. Funct. Mater.* **29**, 1900790 (2019).
14. Liu, P., Han, J., Zhu, K., Dong, Z. & Jiao, L. Heterostructure $SnSe_2$ /ZnSe@PDA nanobox for stable and highly efficient sodiumion storage. *Adv. Energy Mater.* **10**, 2000741 (2020).
15. Chen, S., Ao, Z., Sun, B., Xie, X. & Wang, G. Porous carbon nanocages encapsulated with tin nanoparticles for high performance sodium-ion batteries. *Energy Storage Mater.* **5**, 180–190 (2016).
16. Yang, G. et al. Carbon-based alloy-type composite anode materials toward sodium-ion batteries. *Small* **15**, 1900628 (2019).
17. Zhu, Z. et al. Ultrasmall Sn nanoparticles embedded in nitrogen-doped porous carbon as high-performance anode for lithium-ion batteries. *Nano Lett.* **14**, 153–157 (2014).
18. Park, J. H. et al. Self-assembly of pulverized nanoparticles: an approach to realize large-capacity, long-lasting, and ultra-fast-chargeable Na-ion batteries. *Nano Lett.* **21**, 9044–9051 (2021).
19. Chen, J. et al. Electrolyte design for LiF-rich solid–electrolyte interfaces to enable high-performance microsized alloy anodes for batteries. *Nat. Energy* **5**, 386–397 (2020).
20. Li, A. M. et al. High voltage electrolytes for lithium-ion batteries with micro-sized silicon anodes. *Nat. Commun.* **15**, 1206 (2024).
21. Zhou, L. et al. Electrolyte engineering enables high stability and capacity alloying anodes for sodium and potassium ion batteries. *ACS Energy Lett.* **5**, 766–776 (2020).
22. Huang, J. et al. Nanostructures of solid electrolyte interphases and their consequences for microsized Sn anodes in sodium ion batteries. *Energy Environ. Sci.* **12**, 1550–1557 (2019).
23. Du, X. et al. Stabilizing microsized Sn anodes for Na-ion batteries with extended ether electrolyte chemistry. *ACS Appl. Energy Mater.* **5**, 2252–2259 (2022).
24. Zhang, B. et al. Microsized Sn as advanced anodes in glyme-based electrolyte for Na-ion batteries. *Adv. Mater.* **28**, 9824–9830 (2016).
25. Yao, Q. et al. Intermolecular cross-linking reinforces polymer binders for durable alloy-type anode materials of sodium-ion batteries. *Adv. Energy Mater.* **13**, 2202939 (2022).
26. Mu, P. et al. A spidroin-inspired hierarchical-structure binder achieves highly integrated silicon-based electrodes. *Adv. Mater.* **35**, e2303312 (2023).
27. Zhang, W. et al. Recovery of isolated lithium through discharged state calendar ageing. *Nature* **626**, 306–312 (2024).

28. Yang, Y. et al. Capacity recovery by transient voltage pulse in silicon-anode batteries. *Science* **386**, 322–327 (2024).
29. Liu, F. et al. Dynamic spatial progression of isolated lithium during battery operations. *Nature* **600**, 659–663 (2021).
30. Park, S.-H. et al. High areal capacity battery electrodes enabled by segregated nanotube networks. *Nat. Energy* **4**, 560–567 (2019).
31. He, Z. et al. Advances in carbon nanotubes and carbon coatings as conductive networks in silicon-based anodes. *Adv. Funct. Mater.* **34**, 2408285 (2024).
32. He, Z., Zhang, C., Zhu, Y. & Wei, F. The acupuncture effect of carbon nanotubes induced by the volume expansion of silicon-based anodes. *Energy Environ. Sci.* **17**, 3358–3364 (2024).
33. Jia, H. et al. Hierarchical porous silicon structures with extraordinary mechanical strength as high-performance lithium-ion battery anodes. *Nat. Commun.* **11**, 1474 (2020).
34. Li, Y., Duan, X., Qian, Y., Yang, L. & Liao, H. Nanocrystalline silver particles: synthesis, agglomeration, and sputtering induced by electron beam. *J. Colloid Interface Sci.* **209**, 347–349 (1999).
35. Levitas, V. I. Mechanochemical mechanism for reaction of aluminium nano- and micrometre-scale particles. *Phil. Trans. A Math. Phys. Eng Sci* **371**, 20120215 (2013).
36. Iijima, S. Helical microtubules of graphitic carbon. *Nature* **354**, 56–58 (1991).
37. Biercuk, M. J., Ilani, S., Marcus, C. M. & McEuen, P. L. in *Carbon Nanotubes: Advanced Topics in the Synthesis, Structure, Properties and Applications* 13–16 (Springer, 2008).
38. Dressler, R. A. & Dahn, J. R. Optimization of Si-containing and SiO based anodes with single-walled carbon nanotubes for high energy density applications. *J. Electrochem. Soc.* **171**, 030520 (2024).
39. Yao, Z., Kane, C. L. & Dekker, C. High-field electrical transport in single-wall carbon nanotubes. *Phys. Rev. Lett.* **84**, 2941–2944 (2000).
40. Guoping, W., Qingtang, Z., Zuolong, Y. & Meizheng, Q. The effect of different kinds of nano-carbon conductive additives in lithium ion batteries on the resistance and electrochemical behavior of the $LiCoO_2$ composite cathodes. *Solid State Ion.* **179**, 263–268 (2008).
41. Dressler, R. & Dahn, J. R. Optimization of Si-containing and SiO based anodes with single-wall carbon nanotubes for high energy density applications. *J. Electrochem. Soc.* **171**, 030520 (2024).
42. Mohs hardness test. *Rocks and Minerals* http://www.rocksandminerals.com/hardness/mohs.htm (1995).
43. Lu, Y., Huang, J. Y., Wang, C., Sun, S. & Lou, J. Cold welding of ultrathin gold nanowires. *Nat. Nanotechnol.* **5**, 218–224 (2010).
44. Suryanarayana, C. Mechanical alloying and milling. *Prog. Mater. Sci.* **46**, 1–184 (2001).
45. Sellers, M. S., Schultz, A. J., Basaran, C. & Kofke, D. A. Atomistic modeling of β-Sn surface energies and adatom diffusivity. *Appl. Surf. Sci.* **256**, 4402–4407 (2010).
46. Eckold, P., Sellers, M. S., Niewa, R. & Hügel, W. The surface energies of β-Sn—a new concept for corrosion and whisker mitigation. *Microelectron. Reliab.* **55**, 2799–2807 (2015).
47. Shi, S., Liu, C., Wan, J. & Cui, S. Heterogeneous coherent interface thermodynamics and Wulff construction associated with the cubic-tetragonal-orthorhombic multi-step structural transition in Mn-Ni alloys. *J. Alloys Compd.* **771**, 254–267 (2019).
48. Alsulami, Q. A. & Rajeh, A. Synthesis of the SWCNTs/TiO_2 nanostructure and its effect study on the thermal, optical, and conductivity properties of the CMC/PEO blend. *Results Phys.* **28**, 104675 (2021).
49. Rajeh, A., Morsi, M. A. & Elashmawi, I. S. Enhancement of spectroscopic, thermal, electrical and morphological properties of polyethylene oxide/carboxymethyl cellulose blends: combined FT-IR/DFT. *Vacuum* **159**, 430–440 (2019).
50. Zheng, C. et al. Electrostatic shielding boosts electrochemical performance of alloy-type anode materials of sodium-ion batteries. *Angew. Chem. Int. Ed. Engl.* **62**, e202214258 (2023).
51. Yao, Q. et al. Superior sodiophilicity and molecule crowding of crown ether boost the electrochemical performance of all-climate sodium-ion batteries. *Proc. Natl Acad. Sci. USA* **121**, e2312337121 (2024).
52. Zhu, Z. et al. Avoiding electrochemical indentations: a CNT-cocooned $LiCoO_2$ electrode with ultra-stable high-voltage cycling. *Energy Environ. Sci.* **17**, 6102–6112 (2024).
53. Melitz, W., Shen, J., Kummel, A. C. & Lee, S. Kelvin probe force microscopy and its application. *Surf. Sci. Rep.* **66**, 1–27 (2011).
54. Kim, Y. H. et al. Enabling 100C fast-charging bulk Bi anodes for Na-ion batteries. *Adv. Mater.* **34**, e2201446 (2022).
55. Ji, Y. et al. In situ probing the origin of interfacial instability of Na metal anode. *Chem* **9**, 2943–2955 (2023).
56. Giri, S. K. & Mellema, G. Measuring the topology of reionization with Betti numbers. *Mon. Not. R. Astron. Soc.* **505**, 1863–1877 (2021).
57. Siddiqi, K. & Pizer, S. *Medial Representations: Mathematics, Algorithms and Applications* (Springer, 2008).
58. Edelsbrunner, H. & Harer, J. *Computational Topology: An Introduction* (American Mathematical Society, 2010).
59. Arganda-Carreras, I. et al. Trainable Weka Segmentation: a machine learning tool for microscopy pixel classification. *Bioinformatics* **33**, 2424–2426 (2017).
60. Young, K. & Morrison, H. Quantifying microglia morphology from photomicrographs of immunohistochemistry prepared tissue using ImageJ. *J. Vis. Exp.* **136**, e57648 (2018).

Acknowledgements

This work was supported by the National Key R&D Program of China (2022YFB3807800, Y. Lu), National Natural Science Foundation of China (52394170-52394174, Y.-S.H.; 22339001, F.X.), Commanding heights of science and technology of Chinese Academy of Science (LDES15 0000, Y.-S.H.), Strategic Priority Research Program of the Chinese Academy of Sciences (XDA0400000, Y.-S.H.), International Partnership Program of Chinese Academy of Sciences (005GJHZ2023021MI, Y.-S.H.), Beijing-Tianjin-Hebei Basic Research Cooperation Project (B2024208091, F.X.) and 10th Young Elite Scientists Sponsorship Program by CAST (F.X.). We thank X. Li at the Institutional Center for Shared Technologies and Facilities of Institute of Process Engineering, Chinese Academy of Sciences, for the help in taking and processing FIB-SEM (Avizo) characterizations and analysis.

Author contributions

Z.C., Yuqi Li, F.X. and Y.-S.H. designed this work. Z.C. prepared the Sn-based anode electrodes and carried out the electrochemical experiments, materials characterization (OM, XPS, SEM, TEM, STEM, FT-IR, ECD, topological analysis and machine learning) and data analysis. B.W. performed the DSC and DEMS measurements and analysis. L.W. performed the first-principle calculations. Huajun Li assisted in preparing the single-layer pouch cell. H.Y., R.D. and J.Z. prepared the Ah-level pouch cells. Z.C., Yuqi Li, F.X. and Y.-S.H. co-wrote the paper. All authors participated in experimental data analysis, results discussions and paper preparation.

Competing interests

The authors declare no competing interests.

Additional information

Supplementary information The online version contains supplementary material available at https://doi.org/10.1038/s41560-026-01974-2.

Correspondence and requests for materials should be addressed to Fei Xie or Yong-Sheng Hu.

Peer review information *Nature Energy* thanks Souman Rudra, Naoaki Yabuuchi and the other, anonymous, reviewer(s) for their contribution to the peer review of this work.